



HAL
open science

Double clad tubular anti-resonant hollow core fiber for nonlinear microendoscopy

Alexandre Kudlinski, A. Cassez, O. Vanvincq, D. Septier, A. Pastre, R. Habert, K. Baudelle, M. Douay, V. Mytskaniuk, V. Tsvirkun, et al.

► **To cite this version:**

Alexandre Kudlinski, A. Cassez, O. Vanvincq, D. Septier, A. Pastre, et al.. Double clad tubular anti-resonant hollow core fiber for nonlinear microendoscopy. *Optics Express*, 2020, 28 (10), pp.15062-15070. 10.1364/OE.389084 . hal-02562695

HAL Id: hal-02562695

<https://hal.science/hal-02562695v1>



Submitted on 14 May 2020

HAL is a multi-disciplinary open access archive for the deposit and dissemination of scientific research documents, whether they are published or not. The documents may come from teaching and research institutions in France or abroad, or from public or private research centers.

L'archive ouverte pluridisciplinaire **HAL**, est destinée au dépôt et à la diffusion de documents scientifiques de niveau recherche, publiés ou non, émanant des établissements d'enseignement et de recherche français ou étrangers, des laboratoires publics ou privés.



Double clad tubular anti-resonant hollow core fiber for nonlinear microendoscopy

A. KUDLINSKI,^{1,*}  A. CASSEZ,¹ O. VANVINCQ,¹ D. SEPTIER,¹ A. PASTRE,¹ R. HABERT,¹ K. BAUELLE,¹ M. DOUAY,¹ V. MYTSKANIUK,² V. TSVIRKUN,²  H. RIGNEAULT,² AND G. BOUWMANS¹

¹University of Lille, CNRS, UMR 8523-PhLAM-Physique des Lasers Atomes et Molécules, Lille, France

²Aix Marseille Univ, CNRS, Centrale Marseille, Institut Fresnel, Marseille, France

*alexandre.kudlinski@univ-lille.fr

Abstract: We report the fabrication and characterization of the first double clad tubular anti-resonant hollow core fiber. It allows to deliver ultrashort pulses without temporal nor spectral distortions in the 700-1000 nm wavelength range and to efficiently collect scattered light in a high numerical aperture double clad. The output fiber mode is shaped with a silica microsphere generating a photonic nanojet, making it well suitable for nonlinear microendoscopy application. Additionally, we provide an open access software allowing to find optimal drawing parameters for the fabrication of tubular hollow core fibers.

© 2020 Optical Society of America under the terms of the [OSA Open Access Publishing Agreement](#)

1. Introduction

A major issue in early cancer diagnostic is the identification of potential tumors that requires the careful preparation and inspection of *ex vivo* tissue biopsies by standard histology (haematoxylin, eosin and saffron (HES) staining). Because biopsy removal and histology are labour and time consuming, and therefore delay decision making, surgery and post treatment, there is a need to develop intra-operative *in vivo* imaging tools to provide immediate cancer diagnostics. In this scope, flexible label-free multimodal nonlinear microendoscopes have been reported [1–8]. They combine advantages of nonlinear imaging or spectroscopic techniques with the high compactness and deep penetration ability of flexible endoscopes. In order to get as much information as possible, the endoscope must be ideally capable of performing two photon excitation (TPEF), second (SHG) and third (THG) harmonic generation as well as coherent anti-Stokes Raman scattering (CARS) imaging in a single device [9], with performances comparable to those of nonlinear table microscopes in terms of sensitivity, spatial resolution, field of view, etc.

One of the key issues in developing these nonlinear microendoscopes concerns the endoscopic optical fiber itself. Indeed, firstly, the fiber probe is expected to deliver high power ultrashort pulses (typically 100-200 fs) at different wavelengths over several meters. In the case of TPEF and SHG modalities, Ti:Sa oscillators are usually used in the 750-850 nm spectral range. For CARS imaging, an additional short pulse has to be synchronized to match the vibrational frequency of the molecule to be probed [10] and it is convenient to use continuously tunable optical parametric oscillators (OPOs) delivering both pulses [11]. CARS is often used for lipid imaging, with molecular bonds in the region of 2900 cm^{-1} , which corresponds to wavelength separation of about 200 nm between the two CARS pulses (typically 800 nm and 1040 nm) [12]. The endoscope fiber must therefore be able to deliver short pulses over the 700-1100 nm spectral region, with no spectral nor temporal distortion. Secondly, the output mode of the fiber must be shaped correctly to be focused with the distal optics of the endoscope onto a diffraction limited spot, ensuring optimal spatial resolution. Last, the same fiber must be able to collect the nonlinear signals (TPEF, SHG, THG, CARS) scattered from the biological tissue with the highest possible

collection efficiency, in the visible spectral range (typically between 400 and 650 nm, depending on the imaging modality), and to guide them back to the various detection channels (PMTs). This signal collection is optimally achieved by using a high numerical aperture (NA) double cladding surrounding the fiber core [1–4,6,8]. The simplified architecture of such a multimodal nonlinear microendoscope is schematized in Fig. 1.

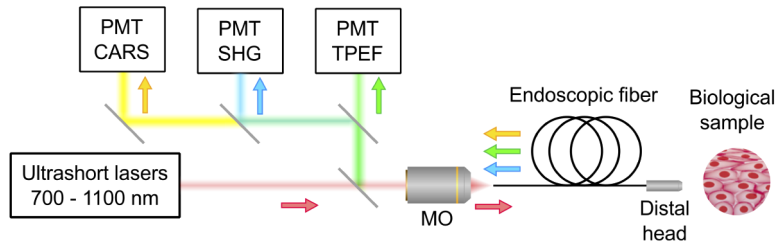


Fig. 1. Scheme of a multimodal nonlinear microendoscope system. MO: microscope objective.

Among possible solutions to match these specifications, double clad hollow core fibers (HCFs) appear promising because light travels in air, with (potentially) lower dispersion and lower nonlinearity than in solid core fibers. Photonic bandgap guiding HCFs suffer from relatively high group velocity dispersion (GVD) and relatively narrow transmission bands, so despite successful laboratory demonstrations [13], they are not well adapted for this purpose, or require additional collection fiber [14]. As for HCFs guiding via inhibited coupling mechanism (Kagome HCFs [15] without or with hypocycloid core contour [16], tubular anti-resonant HCFs [17]), they exhibit very low GVD and nonlinearity [15,17,18], so they are very well suited for the delivery of high power ultrashort pulses [18–20]. Double clad Kagome HCFs have therefore been successfully used in the context of nonlinear microendoscopy [6]. However, due to the important size of air/silica Kagome lattice required for efficient guidance, the collecting area guiding light via total internal reflection consists in a relatively thin silica ring (of less than 40 μm thickness), furthermore it has to be located quite far away ($\sim 100 \mu\text{m}$) from the central core [6,21]. This strongly limits the overall surface collection (to about 21 000 μm^2 in [6] and 12 000 μm^2 in [21]) and thus the collection efficiency of the double clad. This issue can be partly overcome using tubular anti-resonant HCFs for which the microstructured cladding consists in a single layer of capillaries. Therefore, a double clad can be located much closer to the main core, and its surface can be easily enhanced while keeping an outer diameter sufficiently small for a flexible fiber. Such fibers were also successfully used to deliver ultrashort pulses in the context of nonlinear fiber-based microscopy [14,22,23], but the lack of double clad prevented them to be used in an endoscopic configuration. Moreover, their transmission window was not large enough to deliver the two pulses detuned by 3000 cm^{-1} required for CARS experiments. A double clad tubular HCF operating in the 700-1100 nm spectral band would therefore be highly desirable for the development of efficient nonlinear microendoscopic probes.

To address all these issues, we report here the first fabrication and characterization of a double clad tubular anti-resonant HCF. Its transmission spectrum covers the 700-1600 nm spectral range with a low GVD, making it suitable for use in TPEF, SHG, THG and CARS nonlinear endoscopic imaging experiments. Additionally, the fiber has been functionalized to transform the original output fundamental mode with a large mode field diameter (MFD) and low NA into a near diffraction limited spot, making it compatible with miniature distal imaging probes [6,24].

2. Fiber design and fabrication

As discussed above, the use of a tubular anti-resonant HCF in microendoscopy imposes strong requirements in terms of optical properties but also in terms of geometry, because in addition to the main hollow core, the properties of the cladding have to be optimized too. More specifically, a miniature scanner is required to perform imaging. One way of doing this is to place the fiber into a piezoelectric ceramic tube which is driven at a frequency corresponding to the resonant mechanical frequency of the fiber [2]. For compactness requirements, the inner diameter of this ceramic tube must be around 500 μm . Therefore, the outer diameter of the coated fiber must be slightly less than 500 μm , but as close as possible to this value. This dictates the specification for the outer silica cladding diameter: the thickness of the polymer coating has to be large enough to ensure good mechanical properties, but a too large polymer coating thickness means a reduced silica cladding, which is detrimental for the collection of the nonlinear signal. To find a compromise between these two constraints, we chose to fix the outer diameter of the silica cladding to 250 μm , so that the total thickness of polymer coating will be about 125 μm .

We have seen that the hollow core needs to efficiently transmit ultrashort pulses in the range 700-1100 nm. Higher-order antiresonant bands are not broad enough in this wavelength range, so this requires to design a fiber core guiding in the fundamental band, which requires capillary tubes with a < 300 nm thickness in this spectral region [25]. Although challenging, tubular anti-resonant HCFs with such thin cladding tubes have been successfully fabricated [25–27]. Our targeted fiber design therefore follows the design rules deeply investigated and optimized in Ref. [25], in terms of number of tubes, gap size, capillary size and thickness etc. In the present study however, the additional geometrical constraints discussed above slightly complicates the drawing process. In order to identify optimal drawing parameters, and faster than with fastidious trials and errors method, we performed a numerical modeling of the drawing process, using the model recently published in [28] with minor changes (see details in Appendix A). Starting from the dimensions of existing but non-necessarily optimized canes, the model allows to identify optimal drawing parameters (tension, ratio of drawing speeds, core and cladding overpressures) allowing to obtain the targeted fiber structure by avoiding the capillary contact issue described in [28]. A user-friendly version of the software we have developed is available for free download from Appendix A.

We used 2 mm diameter canes jacketed into two tubes so that the outer diameter of the final preform is 7.8 mm. The fiber was drawn at an outer diameter of 250 μm with a draw speed of 9.7 m/min for a feed of 10 mm/min, at a tension of 1 kg and a differential pressure between the core and capillaries of 118 mbar. The model described above was used to identify a rough set of initial parameters, which were slightly adjusted in real time during the drawing process to match the targeted structure. The actual parameters differ from the theoretical ones by a few percent.

3. Fiber characterization

3.1. Transmission properties

Figure 2(a) shows a scanning electron microscope (SEM) image of one of the fabricated tubular anti-resonant HCFs. The double clad is obtained by adding a 35 μm thick layer of low index polymer coating, surrounded by a 90 μm layer of high index, high mechanical resistance polymer coating (both have been removed for acquiring the SEM image). The core diameter is 30 μm and the average capillary thickness is about 250 nm. The distance between capillaries is 5 ± 1 μm and their diameter is 12.6 ± 0.7 μm . The attenuation spectrum measured by cutback (from 30 to 3 m) using a supercontinuum source is displayed in solid blue line in Fig. 2(b) for a selective excitation of the fundamental mode. The fundamental band spans from 650 to 1650 nm, with a loss level lower than 0.2 dB/m between 670 and 1500 nm, which covers the whole tunability range of Ti:Sa oscillators and Yb-doped fiber lasers usually used in nonlinear microendoscopy. The GVD

measured with a low-coherence interferometer is displayed in red full circles in Fig. 2(b) (the solid red line is a polynomial fit). It is less than 2 ps/nm/km in the 700-1100 nm spectral range, which is highly favorable for the delivery of ultrashort pulses.

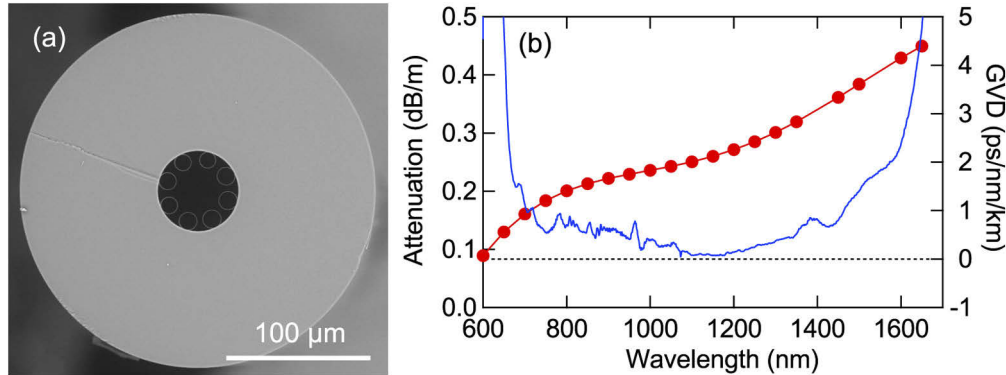


Fig. 2. (a) SEM image of the double clad tubular anti-resonant HCF. The double layer of polymer coating has been removed. (b) Attenuation spectrum (left axis, blue line) and GVD (right axis, red markers and red line) measured across the fundamental band.

3.2. Output mode and fiber functionalization

Although the fabricated HCF is intrinsically multimode, a selective mode excitation at the fiber input allows to couple most of the light in the fundamental mode. Figure 3(b) shows the near field image of the fiber end face at 800 nm. The MFD of the fundamental mode was measured to be 29 μm at 800 nm (at $1/e^2$ of peak intensity) and does not show any significant variation between 700 and 1000 nm. The NA was deduced from the measurement of the $1/e^2$ radius of the far field profile as a function of distance from fiber [blue markers in Fig. 3(e)]. The solid blue line is the linear fit from which the slope gives a NA value of 0.023.

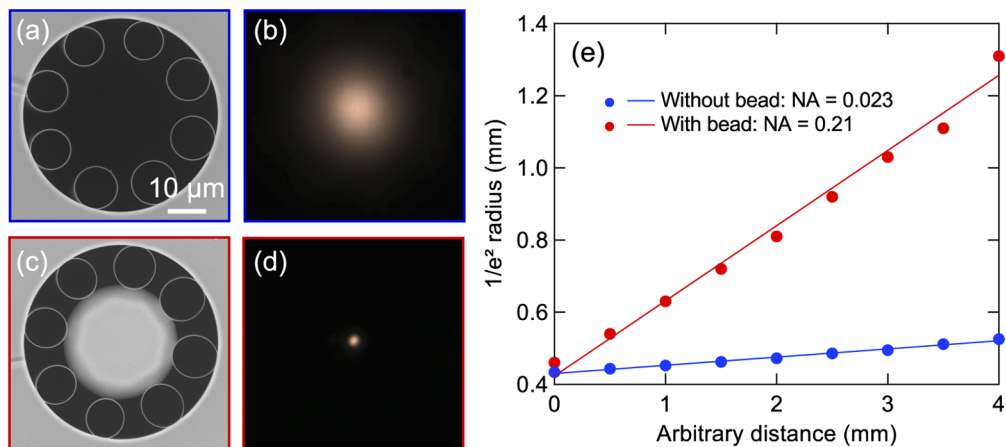


Fig. 3. (a,c) SEM image of the core region (a) without and (c) with silica bead attached. (b,d) Near field mode profile recorded at 800 nm (c) without and (d) with silica bead attached (same scale on (a) to (d) sub-figures). (e) NA measurement at 800 nm without silica bead (blue markers) and with silica bead attached (red markers). Solid lines are linear fits from which the NA value is deduced.

These MFD and NA values are standard for tubular anti-resonant HCF designs [25], but they are problematic for imaging endoscope applications. Indeed, the output fiber mode has to be re-imaged onto the sample with a near diffraction limited spot in order to activate the nonlinear contrast mechanism (TPEF, SHG, THG, CARS) and optimize spatial resolution, with the constraint for the imaging system to be as compact as possible. Starting from a $29\ \mu\text{m}$ MFD at the fiber output would require a $\times 30\text{-}\times 60$ de-magnification to reach a near diffraction limited spot, which would require large focal length lenses, a solution unpractical regarding the final compactness on the endoscope distal head. It results that the output mode of the fiber has to be significantly reduced before being imaged onto the sample. This is done by splicing a silica bead at the fiber output, which generates a photonic nanojet allowing optical confinement at [24] or even below the diffraction limit [29]. This has already been demonstrated with Kagome HCFs, for which the silica microsphere was easily spliced to the hexagonal core contour. Here, by carefully adjusting the heat time and power of the CO_2 laser of the splicer, we show that it is possible to attach a silica bead to the thin capillaries delimiting the core area of tubular anti-resonant HCFs, without substantial deformation of the overall structure. Figure 3(c) shows a SEM image where a $32\ \mu\text{m}$ diameter silica microsphere is spliced to the HCF. The focus spot measured after the bead at $800\ \text{nm}$ is displayed in Fig. 3(d). It corresponds to a point spread function (PSF) with a full width at half maximum (FWHM) of $1.45\ \mu\text{m}$ and NA of 0.21, as shown by red markers and red line in Fig. 3(e). In the final endoscope, this NA value has to be compatible with the one of the miniature distal objective (0.3 in our case). Finally, this focused spot is re-imaged onto the sample with a 0.63 overall magnification of our miniature distal objective finally reaching a near diffraction limited $0.9\ \mu\text{m}$ FWHM spot at the sample plane.

3.3. Double clad

The use of a low index polymer coating allows the silica cladding to guide light via total internal reflection, with a high NA and in a highly multimode way. Figures 4(a) and (b) show respectively the near field and far field images of the fiber end face when the input face is illuminated with a scattered light at $450\ \text{nm}$ (corresponding to the typical spectral range of SHG signals). As can be seen from Fig. 4(a), the whole silica cladding is filled with light, which corresponds to a total collecting area of $46000\ \mu\text{m}^2$. This is more than two times higher than in [6] and almost four times higher than in [21]. Figure 4(c) shows the angular distribution at $450\ \text{nm}$ out of a $2\ \text{m}$ long fiber measured at $50\ \text{cm}$ from the fiber end (markers) and its Gaussian fit (solid line). The $1/e^2$ angle of the Gaussian fit gives a NA value of 0.38 at $450\ \text{nm}$. Note that in the context of an endoscopic application, the collecting efficiency of the endoscope is ultimately limited by the NA of the imaging lenses at the distal end. So ideally, the NA of the double clad should match to the one of the distal optics head.

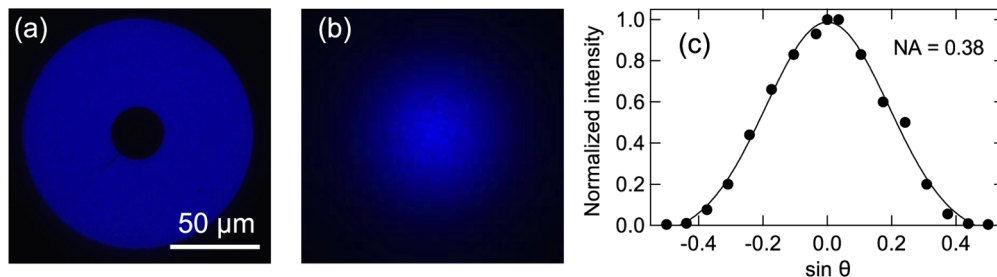


Fig. 4. (a) Near and (b) far field images of the double clad HCF end face obtained with scattered light illumination at $450\ \text{nm}$. (c) Measurement of the output signal at $450\ \text{nm}$ versus angular divergence (markers) and Gaussian fit (solid line).

4. High power ultrashort pulse delivery

Next we investigate the ability of the functionalized [*i.e.* with the silica microsphere Fig. 3(c)] tubular anti-resonant HCF to deliver ultrashort pulses. It is well known that large core ($> 60 \mu\text{m}$) negative curvature HCFs can efficiently deliver intense ultrashort pulses [18–20,30], but here our HCF has a much smaller core and features a silica bead at its output facet. We consider a 2.5 m fiber sample with a silica microsphere attached at the output (same design as previously described). We use a tunable Ti:Sa laser delivering near transformed limited pulses with FWHM duration of 100-200 fs depending on the wavelength. The total transmission of the fiber including coupling efficiency (of 85 %) and silica microsphere is 80 % in the 700-1000 nm spectral range. We did not observe any reduction of transmission efficiency at high average powers (up to 3 W).

Figure 5(a) and (b) compare the evolution of the pulse parameters versus power at the output of a 2.5-m-long HCF sample functionalized with a $32 \mu\text{m}$ diameter silica microsphere spliced at the output (full circles), with the ones of the pulses measured before injection in the fiber (solid horizontal lines), for various Ti:Sa laser wavelengths. The measurements done at the HCF output including a coupling lens, 2.5 m of functionalized HCF and a collimating lens are compared with laser pulses without any optical element. The pulse duration [Fig. 5(a)] measured from the HCF output does not evolve with increasing power, and shows less than 10 % deviation from original pulses, depending on wavelength. The same deviation was observed by removing the silica microsphere. So this slight variation between input and output pulse durations is presumably due to dispersion in the coupling and collimating lenses and to the fact that initial pulses exhibit a slight chirp which changes when the laser is tuned. The output spectral widths displayed in Fig. 5(b) show negligible variation with increasing power and differ by less than 5 % from the initial pulses in each case, indicating that no significant nonlinear effects occurs in the fiber even for average power in the watt level.

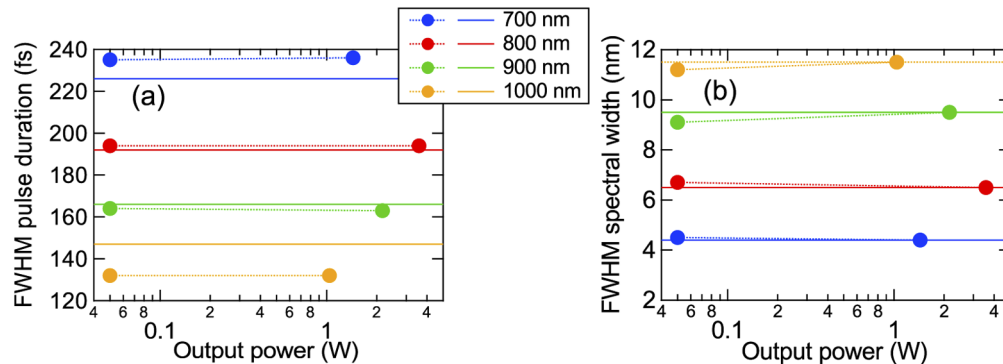


Fig. 5. (a) FWHM pulse duration (full circles) obtained from autocorrelation measurements and (b) FWHM spectral width (full circles) versus output power for various wavelengths of the Ti:Sa laser, in a 2.5 m long HCF with a $32 \mu\text{m}$ diameter silica microsphere spliced at the output. Horizontal solid lines represent the parameters of the Ti:Sa laser pulses before injection in the fiber. See text for details.

These results demonstrate that the splicing of a silica microsphere required to adapt the output fiber mode does not affect the delivery of intense ultrashort pulses required for nonlinear endoscopic imaging. The output power can be higher than 1 W for each wavelength between 700 and 1000 nm (corresponding to a peak power higher than 50 kW), and even reaches 3.6 W ($> 200 \text{ kW}$ peak) at 800 nm, which is by far suitable for efficient nonlinear imaging.

5. Imaging

Finally we integrated the presented functionalized fiber into the setup schematized in Fig. 1 and detailed in [6]. We used a tunable fs laser (Discovery, Coherent) to perform TPEF and SHG nonlinear imaging of representative tissue such as collagen as seen by SHG [Fig. 6(a)], GFP tagged neurons [Fig. 6(b)] and human skin stratum corneum [Fig. 6(c)] as seen by two photon fluo- and auto-fluorescence, respectively. Although the detailed presentation of the nonlinear endoscope system is beyond the scope of this paper, these images demonstrate the capability of the developed fiber to deliver ultra-short pulses and perform efficient signal collection to achieve high quality nonlinear tissue imaging.

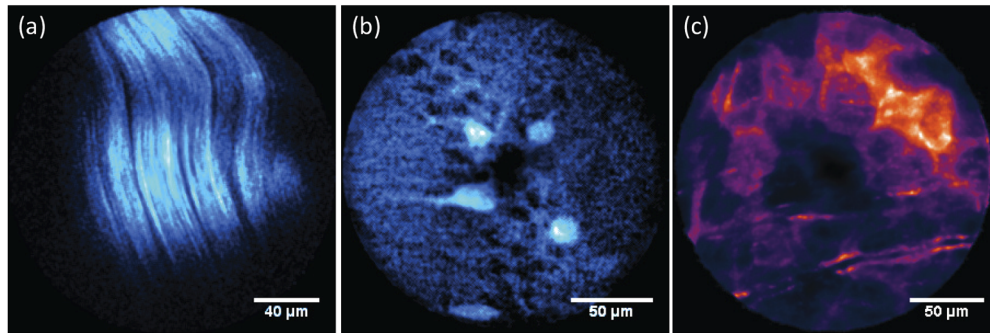


Fig. 6. Nonlinear endoscope imaging using the functionalized NCF: (a) SHG from rat tail tendon collagen (ex: 800 nm, sample power: 30 mW), (b) TPEF from GFP labelled brain slice neurons (ex: 930 nm, sample power 80 mW), (c) autofluorescence from human skin (stratum corneum) (ex: 800 nm, sample power: 100 mW).

6. Conclusion

We have developed a tubular anti-resonant HCF optimized for nonlinear microendoscopes. It has a broad low loss and low GVD transmission band from 650 to 1650 nm suitable to deliver ultrashort pulses from Ti:Sa oscillators but also from Yb-doped fiber lasers or OPOs designed for biophotonics with no temporal nor spectral distortions. It also features a high NA highly multimode double clad allowing to efficiently collect visible light and guide it through total internal reflection. We envision that this functionalized fiber is also suitable to perform CARS and stimulated Raman scattering imaging [31] to enable multimodal nonlinear imaging flexible endoscope developments.

Appendix A

A free MATLAB application has been developed to compute the drawing parameters that allow to obtain a target fiber from a given fabricated cane [32]. The method used in this software is described in the paper of G. T. Jasion *et al.* [28] with two minor modifications:

- (1) Equation (3) of Ref. [28] has been modified as follows to take into account the fact that black body radiation is a surface phenomenon and not a volume one:

$$\frac{(R_j^2 - r_j^2)}{2} \rho c_p w \frac{dT}{dz} = R_j N (T_a - T) + R_j \sigma \alpha (T_a^4 - T^4)$$

- (2) The glass viscosity model is based on [33]

Funding

Agence Nationale de la Recherche (ANR-11-LABX-0007, ANR-11-EQPX-0017, ANR-11-IDEX-0001-02, ANR-11-INSE-0006, ANR-19-CE19-0019); Ministère de l'Enseignement supérieur, de la Recherche et de l'Innovation; Région Hauts-de-France (CPER "Photonics for Society"); Institut National de la Santé et de la Recherche Médicale (Physicancer (18CP128-00)).

Acknowledgments

The fiber was made at FiberTech Lille (<http://fibertech.univ-lille.fr>). We acknowledge D. Labat, A. Cotteret and F. Lédée for splicing of the silica beads and assistance in fiber characterization.

Disclosures

The authors declare no conflicts of interest

References

1. Y. Zhao, H. Nakamura, and R. J. Gordon, "Development of a versatile two-photon endoscope for biological imaging," *Biomed. Opt. Express* **1**(4), 1159 (2010).
2. D. R. Rivera, C. M. Brown, D. G. Ouzounov, I. Pavlova, D. Kobat, W. W. Webb, and C. Xu, "Compact and flexible raster scanning multiphoton endoscope capable of imaging unstained tissue," *Proc. Natl. Acad. Sci.* **108**(43), 17598–17603 (2011).
3. G. Ducourthial, P. Leclerc, T. Mansuryan, M. Fabert, J. Brevier, R. Habert, F. Braud, R. Batrin, C. Vever-Bizet, G. Bourg-Heckly, L. Thiberville, A. Druilhe, A. Kudlinski, and F. Louradour, "Development of a real-time flexible multiphoton microendoscope for label-free imaging in a live animal," *Sci. Rep.* **5**(1), 18303 (2015).
4. W. Liang, G. Hall, B. Messerschmidt, M.-J. Li, and X. Li, "Nonlinear optical endomicroscopy for label-free functional histology in vivo," *Light: Sci. Appl.* **6**(11), e17082 (2017).
5. A. Lukic, S. Dochow, H. Bae, G. Matz, I. Latka, B. Messerschmidt, M. Schmitt, and J. Popp, "Endoscopic fiber probe for nonlinear spectroscopic imaging," *Optica* **4**(5), 496 (2017).
6. A. Lombardini, V. Mytskaniuk, S. Sivankutty, E. R. Andresen, X. Chen, J. Wenger, M. Fabert, N. Joly, F. Louradour, A. Kudlinski, and H. Rigneault, "High-resolution multimodal flexible coherent Raman endoscope," *Light: Sci. Appl.* **7**(1), 10 (2018).
7. B. N. Ozbay, G. L. Futia, M. Ma, V. M. Bright, J. T. Gopinath, E. G. Hughes, D. Restrepo, and E. A. Gibson, "Three dimensional two-photon brain imaging in freely moving mice using a miniature fiber coupled microscope with active axial-scanning," *Sci. Rep.* **8**(1), 8108 (2018).
8. F. Akhouni, Y. Qin, N. Peyghambarian, J. K. Barton, and K. Kieu, "Compact fiber-based multi-photon endoscope working at 1700 nm," *Biomed. Opt. Express* **9**(5), 2326 (2018).
9. S. You, H. Tu, E. J. Chaney, Y. Sun, Y. Zhao, A. J. Bower, Y.-Z. Liu, M. Marjanovic, S. Sinha, Y. Pu, and S. A. Boppart, "Intravital imaging by simultaneous label-free autofluorescence-multiharmonic microscopy," *Nat. Commun.* **9**(1), 2125 (2018).
10. H. Rigneault and P. Berto, "Tutorial: Coherent raman light matter interaction processes," *APL Photonics* **3**(9), 091101 (2018).
11. S. Brustlein, P. Ferrand, N. Walther, S. Brasselet, C. Billaudeau, D. Marguet, and H. Rigneault, "Optical parametric oscillator-based light source for coherent Raman scattering microscopy: practical overview," *J. Biomed. Opt.* **16**(2), 021106 (2011).
12. B. Sarri, R. Canonge, X. Audier, E. Simon, J. Wojak, F. Caillol, C. Cador, D. Marguet, F. Poizat, M. Giovannini, and H. Rigneault, "Fast stimulated raman and second harmonic generation imaging for intraoperative gastro-intestinal cancer detection," *Sci. Rep.* **9**(1), 10052 (2019).
13. S. Brustlein, P. Berto, R. Hostein, P. Ferrand, C. Billaudeau, D. Marguet, A. Muir, J. Knight, and H. Rigneault, "Double-clad hollow core photonic crystal fiber for coherent Raman endoscope," *Opt. Express* **19**(13), 12562–12568 (2011).
14. W. Zong, R. Wu, M. Li, Y. Hu, Y. Li, J. Li, H. Rong, H. Wu, Y. Xu, Y. Lu, H. Jia, M. Fan, Z. Zhou, Y. Zhang, A. Wang, L. Chen, and H. Cheng, "Fast high-resolution miniature two-photon microscopy for brain imaging in freely behaving mice," *Nat. Methods* **14**(7), 713–719 (2017).
15. F. Couny, F. Benabid, and P. S. Light, "Large-pitch kagome-structured hollow-core photonic crystal fiber," *Opt. Lett.* **31**(24), 3574–3576 (2006).
16. Y. Y. Wang, N. V. Wheeler, F. Couny, P. J. Roberts, and F. Benabid, "Low loss broadband transmission in hypocycloid-core Kagome hollow-core photonic crystal fiber," *Opt. Lett.* **36**(5), 669–671 (2011).
17. C. Wei, R. J. Weiblen, C. R. Menyuk, and J. Hu, "Negative curvature fibers," *Adv. Opt. Photonics* **9**(3), 504–561 (2017).

18. A. N. Kolyadin, G. K. Alagashev, A. D. Pryamikov, L. Mouradian, A. Zeytunyan, H. Toneyan, A. F. Kosolapov, and I. A. Bufetov, "Negative Curvature Hollow-core Fibers: Dispersion Properties and Femtosecond Pulse Delivery," *Phys. Procedia* **73**, 59–66 (2015).
19. Y. Wang, M. Alharbi, T. D. Bradley, C. Fourcade-Dutin, B. Debord, B. Beaudou, F. Gérôme, and F. Benabid, "Hollow-core photonic crystal fibre for high power laser beam delivery," *High Power Laser Sci. Eng.* **1**(1), 17–28 (2013).
20. B. Debord, M. Alharbi, L. Vincetti, A. Husakou, C. Fourcade-Dutin, C. Hoenninger, E. Mottay, F. Gérôme, and F. Benabid, "Multi-meter fiber-delivery and pulse self-compression of milli-Joule femtosecond laser and fiber-aided laser-micromachining," *Opt. Express* **22**(9), 10735–10746 (2014).
21. F. Delahaye, M. Maurel, M. Chafer, F. Amrani, B. Debord, F. Gérôme, and F. Benabid, "Double-clad hypocycloid core-contour Kagome hollow-core photonic crystal fiber," in *Conference on Lasers and Electro-Optics*, (OSA, San Jose, California, 2018), p. JTh2A.97.
22. B. Sherlock, F. Yu, J. Stone, S. Warren, C. Paterson, M. A. A. Neil, P. M. W. French, J. Knight, and C. Dunsby, "Tunable fibre-coupled multiphoton microscopy with a negative curvature fibre," *J. Biophotonics* **9**(7), 715–720 (2016).
23. B. Sherlock, S. C. Warren, Y. Alexandrov, F. Yu, J. Stone, J. Knight, M. A. A. Neil, C. Paterson, P. M. W. French, and C. Dunsby, "In vivo multiphoton microscopy using a handheld scanner with lateral and axial motion compensation," *J. Biophotonics* **11**(2), e201700131 (2018).
24. P. Ghenuche, H. Rigneault, and J. Wenger, "Photonic nanojet focusing for hollow-core photonic crystal fiber probes," *Appl. Opt.* **51**(36), 8637 (2012).
25. B. Debord, A. Amsanpally, M. Chafer, A. Baz, M. Maurel, J. M. Blondy, E. Hugonnot, F. Scol, L. Vincetti, F. Gérôme, and F. Benabid, "Ultralow transmission loss in inhibited-coupling guiding hollow fibers," *Optica* **4**(2), 209–217 (2017).
26. S.-f. Gao, Y.-y. Wang, X.-l. Liu, C. Hong, S. Gu, and P. Wang, "Nodeless hollow-core fiber for the visible spectral range," *Opt. Lett.* **42**(1), 61–64 (2017).
27. F. Yu, M. Cann, A. Brunton, W. Wadsworth, and J. Knight, "Single-mode solarization-free hollow-core fiber for ultraviolet pulse delivery," *Opt. Express* **26**(8), 10879–10887 (2018).
28. G. T. Jasion, J. R. Hayes, N. V. Wheeler, Y. Chen, T. D. Bradley, D. J. Richardson, and F. Poletti, "Fabrication of tubular anti-resonant hollow core fibers: modelling, draw dynamics and process optimization," *Opt. Express* **27**(15), 20567–20582 (2019).
29. A. Devilez, N. Bonod, J. Wenger, D. Gérard, B. Stout, H. Rigneault, and E. Popov, "Three-dimensional subwavelength confinement of light with dielectric microspheres," *Opt. Express* **17**(4), 2089 (2009).
30. D. Dobrakowski, A. Rampur, G. Stepniewski, D. Pysz, L. Zhao, Y. Stepanenko, R. Buczynski, and M. Klimczak, "Femtosecond pulse delivery around 1560 nm in large-core inhibited-coupling fibers," *J. Opt. Soc. Am. B* **36**(11), 3030–3038 (2019).
31. A. Lombardini, E. R. Andresen, A. Kudlinski, I. Rimke, and H. Rigneault, "Origin and suppression of parasitic signals in kagomé lattice hollow core fibers used for SRS microscopy and endoscopy," *Opt. Lett.* **42**(9), 1824 (2017).
32. O. Vanvincq, "HARF-drawing," <https://doi.org/10.5281/zenodo.3582197> (2019).
33. A. Kondratiev and A. Khvan, "Analysis of viscosity equations relevant to silicate melts and glasses," *J. Non-Cryst. Solids* **432**, 366–383 (2016).